ADVANCED OPTICAL MATERIALS
www.advopticalmat.de

Electrically Tunable Strong Optical Nonlinearity in Near-Infrared by Coupled Metallic Quantum Wells

*Ching-Fu Chen, Haoliang Qian, and Zhaowei Liu**

An electrically tunable nonlinear optical device working at near-infrared wavelength is theoretically and experimentally demonstrated. Ultrahigh optical second-order nonlinearity from titanium-nitride-based coupled metallic quantum wells can be electrically tuned by external electric field. Tunability of second-order susceptibility $\chi^{(2)}$ reaches a 63% modulation depth with an average tunability of 10.5% per volt. In addition, electro-optic modulation of second-harmonic signal is presented by continuous tuning of $\chi^{(2)}$ over a long period of time with high stability. These results provide a new material platform with actively controllable strong nonlinearity for future nonlinear photonic systems, such as ultra-compact opto-electronic modulation devices and reconfigurable nonlinear metamaterials and metasurfaces.

1. Introduction

Nonlinear optics is a rapidly growing field of research, driven by advances in ultrafast laser, material science, and nanotechnology in the past decades.[1] The nonlinear response of light-matter interaction can lead to interesting phenomena such as harmonic generation, self-focusing, and optical switching, which further develop into a variety of important applications in areas of laser technology, imaging, sensing, spectroscopy, and telecommunications. In general, optical nonlinearity of natural materials is weak and non-tunable, which hinders the usage of nonlinear optics in many practical scenarios.

Coupled quantum wells system is an appealing candidate for strong and tunable optical nonlinearity, receiving much attention recently. Semiconductor multi-quantum-well has been investigated to show high second-order susceptibility $\chi^{(2)}$ in the mid-infrared (MIR) regime.[2–4] In other studies, its tunability has also been proven via resonant Stark tuning of the optical intersubband transitions (ISBTs), while the working wavelengths fall in the far-infrared range.[5,6] More recently, engineered optical ISBTs in n-doped multi-quantum-well semiconductor heterostructures were combined with tailored plasmonic metasurfaces for giant[7–11] and electrically controllable[12] second-order nonlinear optical response. Yet, all these demonstrations are in the long wavelength regime due to the relatively small band offsets in the selected semiconductor heterostructures.

On the other hand, nonlinear optics in the visible and near-infrared (NIR) wavelengths play an important role in the development of modern science and technology, including various applications such as nonlinear plasmonic sensing,[13] nonlinear microscopy for biomolecules,[14,15] geometrical characterization of nanostructures and atomic monolayers,[16–18] and electro-optic modulators.[19–23] In a recent work, we presented an unprecedented record-high $\chi^{(2)}$ of 1500 pm V^{-1} in NIR using titanium nitride (TiN) based coupled metallic quantum wells (cMQWs).[24] The TiN/Al_2O_3 heterostructures have exceptionally large band offset (≈8 eV), supporting multiple ISBTs covering spectrum range from MIR all the way to ultraviolet. In addition, both TiN and Al_2O_3 are refractory materials with very high damage threshold which is especially suitable for high-power nonlinear optics.[25]

Besides pursuing strong nonlinearity, realizing tunable nonlinearity is also significantly important because it enables one to manipulate nonlinear response unattainable in natural materials and to facilitate reconfigurable nonlinear metamaterials and metasurfaces. It is worth noting that scientists have been seeking after different methods to dynamically control optical nonlinearity in various material systems in the NIR range. Several works have been published, such as plasmonic enhanced electric-field induced second-harmonic (EFISH) that electrically tunes effective $\chi^{(2)}$ which originates from third-order nonlinearity and DC electric field $\chi^{(3)}E_{\mathrm{control}}$,[26–28] plasmonic-enhanced charge-assisted second-harmonic (p-CASH) that tunes nonlinear polarization $\chi^{(2)}E_{\omega}E_{\omega}$ by electrically controlling the plasmonic enhancement,[29] field-induced second-order nonlinearity in CdS nanobelt that creates nonlinear dipole moment by applying high electric field to distort electron wave function,[30] and tunable SHG in transition metal dichalcogenides (TMDs) that controls second-order nonlinearity by tuning exciton resonance or breaking inversion symmetry either electrically or optically.[31–34]

C.-F. Chen, H. Qian, Z. Liu
Department of Electrical and Computer Engineering
University of California San Diego
9500 Gilman Drive, La Jolla, San Diego, CA 92093, USA
E-mail: zhaowei@ucsd.edu
Z. Liu
Materials Science and Engineering Program
University of California San Diego
9500 Gilman Drive, La Jolla, San Diego, CA 92093, USA
Z. Liu
Center for Memory and Recording Research
University of California San Diego
9500 Gilman Drive, La Jolla, San Diego, CA 92093, USA

The ORCID identification number(s) for the author(s) of this article can be found under https://doi.org/10.1002/adom.202302176

DOI: 10.1002/adom.202302176

However, none of these works achieves direct modification of ultrahigh $\chi^{(2)}$ such as that in our metallic quantum wells.

In this paper, we demonstrate both theoretically and experimentally the tunability of strong optical second-order nonlinearity in our TiN-based cMQWs system. By applying an external electric field to the cMQWs via a bias voltage, misalignment will be introduced to the doubly-resonant ISBTs, and thus, the ultrahigh $\chi^{(2)}$ can be electrically controlled. For the first time to our knowledge, a quantum-engineered electrically-tunable nonlinear optical device working at NIR wavelength is accomplished. Our findings pave the way toward a new platform for on-chip opto-electronic modulation devices and reconfigurable nonlinear metamaterials and metasurfaces in the near future.

2. Results and Discussion

2.1. Theoretical Model for Electrically Tunable Nonlinearity

Figure 1a shows the schematic of the optical device used to demonstrate electrically tunable $\chi^{(2)}$. The cMQWs, which behave as an electrically tunable strong nonlinear medium, are sandwiched between a uniform TiN ground plane and a patterned gold (Au) top layer. When a bias voltage is applied, a modulated SHG signal can be observed as a result of tuned second-order nonlinearity $\chi^{(2)}$. For the cMQWs, we adopt the design in our previous work,[24] where one unit of cMQWs consists of TiN/Al_2O_3/TiN coupled asymmetric quantum wells with thickness 1.0/0.5/2.2 nm. Here, the two TiN metallic quantum wells with different thicknesses support three equally spaced electronic subbands, while the middle ultrathin aluminum oxide (Al_2O_3) acts as a dielectric barrier for coupling between the two adjacent quantum wells. A giant $\chi^{(2)}$ peak at NIR wavelength of 920 nm, which carries out SHG at visible wavelength of 460 nm, can be observed with designed double resonant transitions. Detailed calculation of dipole moments and $\chi^{(2)}$ were presented in our previous work.[24]

Figure 1b shows the conduction band diagram of single cMQWs unit at its initial state without external electric field. Electron wavefunctions of the left quantum well (blue) and right quantum well (red) near Fermi level (dotted) are plotted. ISBTs are designed to be perfectly aligned for the double resonant transitions $E_{21} = E_{32} = 1.34$ eV (920 nm) and $E_{31} = 2.68$ eV (460 nm). Under this configuration, the resonance $\chi^{(2)}$ reaches as high as 1500 pm V^{-1} at 920 nm, which has been theoretically and experimentally proven.[24] To implement tunability on top of the strong resonance nonlinearity, external electric field is applied to the cMQWs system through a bias voltage. As shown in Figure 1c, when external electric field of 3 MV cm^{-1} is applied (see the case for reversed bias in the Supporting Information), the 0.5 nm Al_2O_3 barrier tilts by 0.15 eV. E_{21} stays unaltered, but E_{32} lowers to 1.19 eV and E_{31} changes to 2.53 eV correspondingly. Thus, ISBTs are deliberately misaligned to break the established double resonant condition, and $\chi^{(2)}$ peak drops remarkably. Based on the recently proposed quantum electrostatic model,[24,35] $\chi^{(2)}$ spectrum with external electric field dependence is calculated and shown in Figure 1d. The peak becomes weaker and broader as ISBT misalignment gets greater with increasing external electric field. Figure 1e marks the trend of decreasing $\chi^{(2)}$ peak at its original peak wavelength of 920 nm. Notably, $\chi^{(2)}$ drops ≈70% in the presence of 3 MV cm^{-1} of electric field. Such a large $\chi^{(2)}$ with high tunability makes the cMQWs a perfect candidate for tunable nonlinear optical device.

2.2. Design and Simulation for the Tunable Nonlinear Optical Device

Figure 2a shows the unit cell design for the tunable $\chi^{(2)}$ device. This metal–insulator–metal (MIM) plasmonic absorber design is aimed to provide strong absorption of the light at fundamental frequency, convert incident in-plane polarization to effective z-direction, and confine the electric field inside cMQWs layer with large enhancement, thus boost the nonlinear conversion efficiency. Since $\chi^{(2)}$ of the cMQWs layer is dominant in the vertical direction, strong electric field in the z-direction is critical for efficient nonlinear process. In addition, the bottom TiN layer (50 nm) also serves as a bottom electrode, while the top Au layer (30 nm) serves as a top electrode. These electrodes will be used to apply external electric field for tuning at a later stage. Inset of Figure 2a shows more details of the multilayer structure. The cMQWs layer, which consists of two TiN asymmetric metallic quantum wells (1.0 and 2.2 nm) and one ultrathin Al_2O_3 dielectric barrier (0.5 nm), is the main active tuning nonlinear layer providing strong and tunable nonlinearity. The Al_2O_3 layers above and below the cMQWs layer (10 nm) act as insulating layers under the electrical biasing. Numerical simulations in this work are performed with finite element method (FEM) using commercial software COMSOL Multiphysics. Figure 2b shows the simulated reflection and absorption spectra with normal incidence, which results in an absorption peak and a reflection dip at 920 nm, aligning well with the peak $\chi^{(2)}$ value of the cMQWs. Measured reflection result drawn in black dashed line further confirms the design experimentally. Figure 2c,d show the distribution of z-polarized electric field at cross-sectional view and in-plane view, respectively. Color bar indicates the enhancement factor, which is z-component electric field normalized to the magnitude of incident electric field. Owing to the localized surface plasmon resonance of the designed nanostructures, incident electric field is converted from x-direction to z-direction and enhanced by around 7.8-fold at the vicinity of the cMQWs layer for effective nonlinear process.

2.3. Fabrication for the Tunable Nonlinear Optical Device

The cMQWs unit composed of TiN metallic quantum wells and Al_2O_3 dielectric barrier are epitaxially grown by reactive magnetron sputtering using AJA ATC Orion 8 RF Sputtering System. At first, 50 nm of TiN is grown on sapphire substrate to serve as bottom reflective ground plane and bottom electrode. Note that TiN is chosen for the base layer because it not only possesses good electrical conductivity, but also provides perfect lattice matching for the TiN metallic quantum wells to be grown on top subsequently. Details of film growth conditions are discussed in the supplementary section. Then, 10 nm of Al_2O_3 is deposited by atomic layer deposition (ALD) using Beneq TFS200 Atomic Layer Deposition System as insulating layer. Thickness of this insulating layer is designed to optimize both electrical

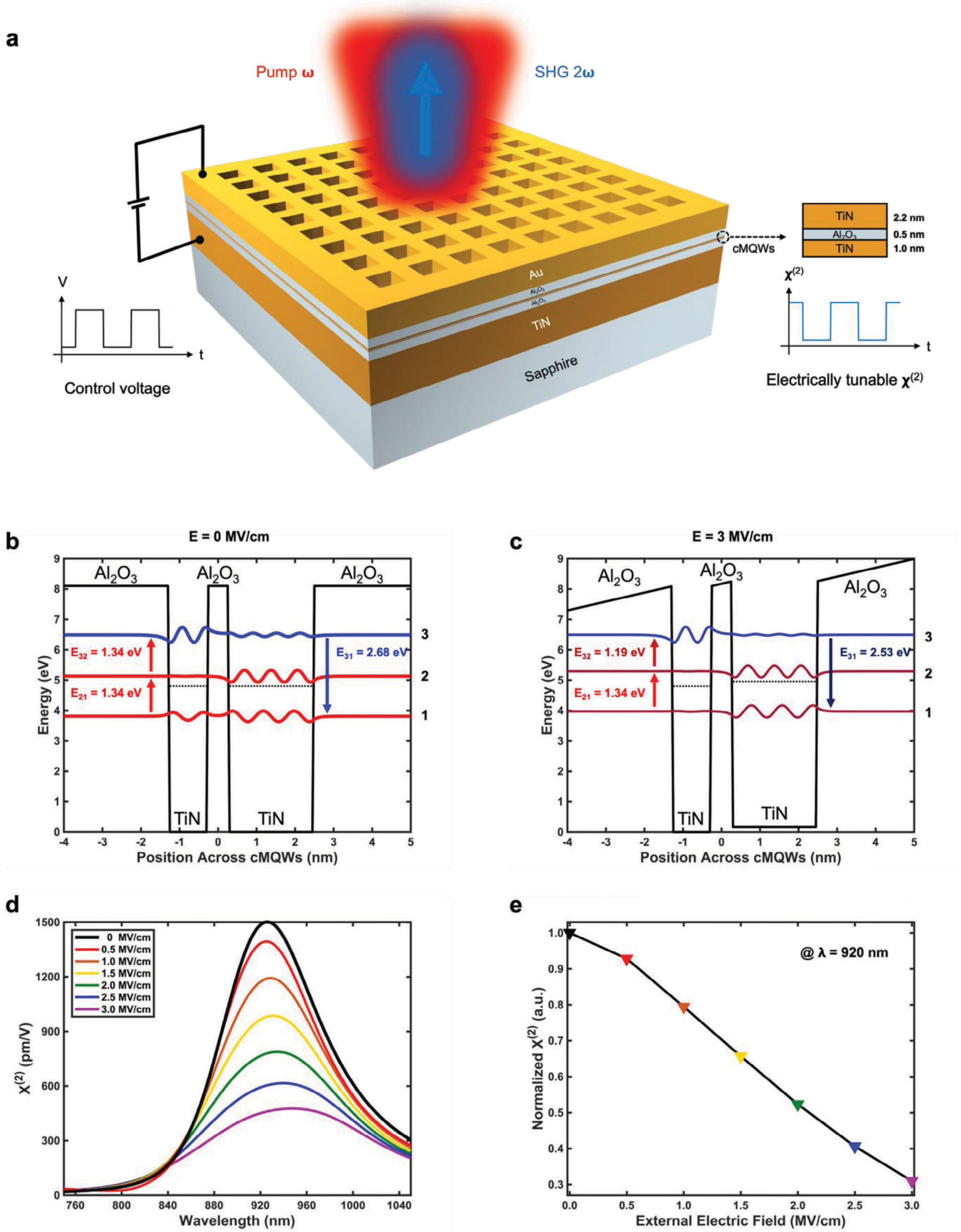
a
Pump ω
SHG 2ω
Au
Al_2O_3
Al_2O_3
TiN
Sapphire
cMQWs
TiN 2.2 nm
Al_2O_3 0.5 nm
TiN 1.0 nm
V
t
Control voltage
$\chi^{(2)}$
t
Electrically tunable $\chi^{(2)}$
b
E = 0 MV/cm
Al_2O_3
Al_2O_3
Al_2O_3
E_{32} = 1.34 eV
E_{21} = 1.34 eV
E_{31} = 2.68 eV
3
2
1
TiN
TiN
Energy (eV)
Position Across cMQWs (nm)
c
E = 3 MV/cm
Al_2O_3
Al_2O_3
Al_2O_3
E_{32} = 1.19 eV
E_{21} = 1.34 eV
E_{31} = 2.53 eV
3
2
1
TiN
TiN
Energy (eV)
Position Across cMQWs (nm)
d
0 MV/cm
0.5 MV/cm
1.0 MV/cm
1.5 MV/cm
2.0 MV/cm
2.5 MV/cm
3.0 MV/cm
$\chi^{(2)}$ (pm/V)
Wavelength (nm)
e
@ λ = 920 nm
Normalized $\chi^{(2)}$ (a.u.)
External Electric Field (MV/cm)

insulating durability and electrical tuning efficiency. That is, the thicker the stronger for electrical insulating, while the thinner the more efficient for electrical tuning. As elaborated in the theoretical section above, tunability of $\chi^{(2)}$ is directly proportional to the electric potential tilt in the barrier Al_2O_3 between the TiN metallic quantum wells, which introduces misalignment to the double resonant transitions. Since the applied voltage drop is equally distributed among the barrier Al_2O_3 and insulator Al_2O_3, total voltage required for the same $\chi^{(2)}$ tuning performance raises when insulator Al_2O_3 gets thicker. Next, the cMQWs layer consists of TiN/Al_2O_3/TiN (1/0.5/2.2 nm) asymmetric metallic quantum wells and ultrathin dielectric barrier are grown by the reactive magnetron sputtering system. Then, another 10 nm of Al_2O_3 insulating layer is deposited by ALD, sandwiching the cMQWs layer between the two insulating layers. After these thin film depositions, Au nanogrid patterns are created by electron

Figure 1. Schematic and theoretical calculation of tunable $\chi^{(2)}$ in cMQWs. a) Schematic of the optical device consisting of cMQWs with electrically tunable $\chi^{(2)}$, which is sandwiched between a uniform TiN film as bottom electrode and a patterned Au film as top electrode. b,c) Conduction band diagram of single TiN-based cMQWs unit. Thickness of TiN/Al_2O_3/TiN asymmetric quantum wells with ultrathin barrier is 1.0/0.5/2.2 nm, respectively. Electron wavefunctions of the left quantum well (blue) and right quantum well (red) near Fermi level (dotted) are plotted. b) ISBTs are perfectly aligned for double resonant transitions at 1.34 eV (920 nm) and 2.68 eV (460 nm) without external electric field. c) When external electric field of 3 MV cm^{-1} is applied, E_{32} drops to 1.19 eV and E_{31} changes to 2.53 eV. d) Calculated $\chi^{(2)}$ spectrum with different external electric field. e) Decreasing trend of $\chi^{(2)}$ peak at 920 nm with increasing external electric field. $\chi^{(2)}$ drops 70% when 3 MV cm^{-1} of electric field is applied.

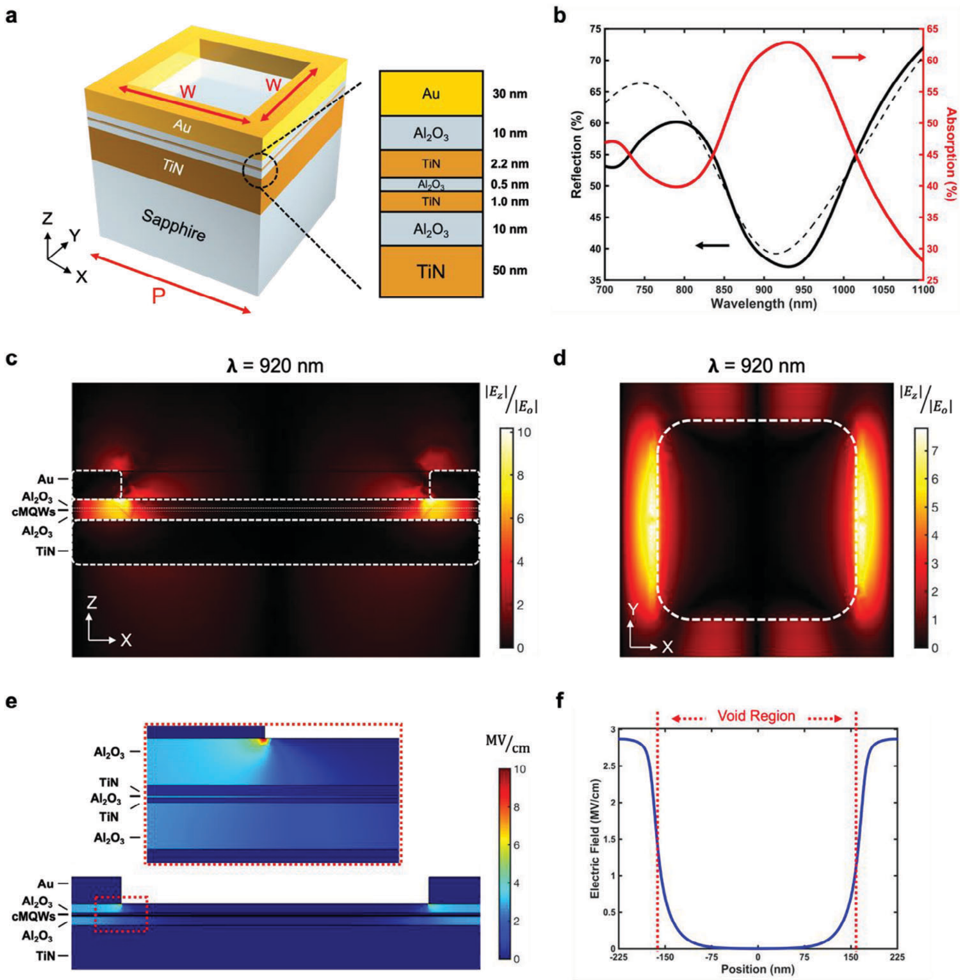

Figure 2. Design and simulated optical response for the tunable $\chi^{(2)}$ device. a) Unit cell for MIM plasmonic absorber design. Top Au nanogrid is 30-nm-thick with tailored parameters: width W = 340 nm and period P = 450 nm. Inset shows the details of each layer and its thickness. b) Simulated reflection (black) and absorption (red) spectra for normal-incident x-polarized light from the top. Designed resonance at fundamental wavelength results in a reflection dip and an absorption peak at 920 nm. Measured reflection (black dashed) is drawn for comparison. c,d) Simulated electric field z-component (E_z) distribution inside the MIM structure in c) cross-sectional view at the center of the unit cell (*x–z* plane) and d) in-plane view at the middle of the 0.5 nm Al_2O_3 barrier layer in cMQWs layer (*x–y* plane). Wavelength is set at 920 nm. Color bar shows field enhancement relative to the incident field, which can reach to as high as 7.8-fold inside the cMQWs layer. e,f) Simulated DC electric field distribution in e) cross-sectional view at the center of the unit cell (*x–z* plane) and f) along x-direction at the middle Al_2O_3 barrier layer. A bias voltage of 6 V is applied via the top Au nanostructure and the bottom TiN plane. Peak of DC electric field at the barrier layer can reach to nearly 3 MV cm^{-1}.

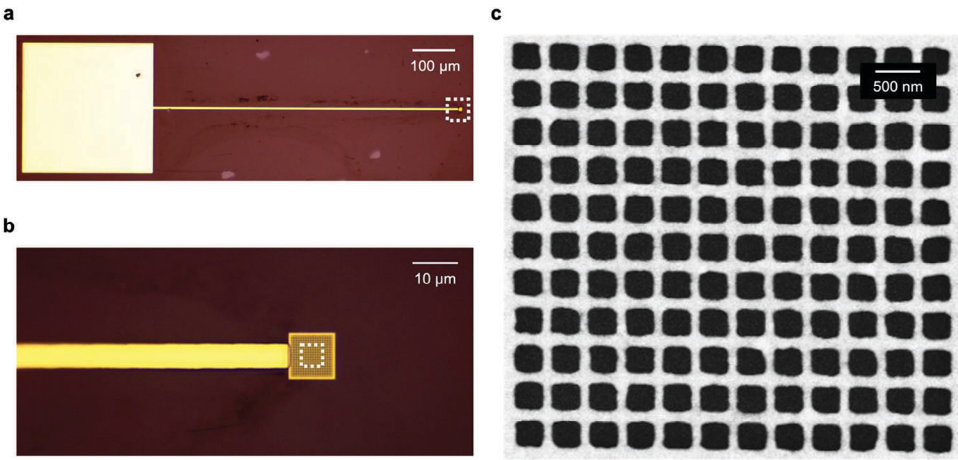

Figure 3. Images of the tunable $\chi^{(2)}$ device. a,b) Optical microscope images of single device, including the Au top electrode (300 µm × 300 µm) and connection to the Au nanogrid pattern (10 µm × 10 µm). b) Zoomed-in view for the marked white square in (a). c) SEM image of the Au nanogrid pattern for the marked white square in (b). Side of the square void is 340 nm while the period is 450 nm, as designed.

beam lithography (EBL) using Vistec EBPG5200 Electron Beam Writer, followed by electron beam evaporation of Au (30 nm) using Temescal BJD-1800 E-beam Evaporator and lift-off process. Finally, Au electrodes are made by photolithography using Heidelberg MLA150 Maskless Aligner, followed by sputtered Al_2O_3 (60 nm), e-beam-evaporated Au (150 nm), and lift-off process. More details for lithography are listed in the supplementary section. **Figure** 3a,b show images of the final device under optical microscope. The Au top electrode is 300 µm × 300 µm in size with an arm stretching out to connect the Au nanogrid which is 10 µm × 10 µm. Design of the Au nanogrid is checked by scanning electron microscope (SEM) image as shown in Figure 3c. Size of the square void is 340 nm while the period is 450 nm. Based on our numerical simulation shown in the above section, this design of Au nanogrid holds strong absorption of fundamental light at 920 nm and thus contributes to the boost of nonlinear conversion efficiency.

2.4. Optical Measurement for Electrically Tunable Nonlinearity

Figure 4a depicts the optical setup for the tunable nonlinearity measurement, where we demonstrate the electrically tunable $\chi^{(2)}$ mechanism by measuring the modulated SHG signal of the device. We use a Ti:Sapphire femtosecond laser (Spectra Physics – Mai Tai HP) with 100 fs pulse width and 80 MHz repetition rate to excite SHG. Excitation filter and emission filter are used to insure both clean fundamental light illumination and second-harmonic signal collection, while the dichroic beam splitter reflects the incoming 920 nm light and transmits the outgoing 460 nm light. A microscope (Olympus – IX81) with 20x objective is used to focus incident light onto Au nanogrid of the device and also collect emitted SHG signal to the Photomultiplier tube (PMT, Hamamatsu – H10721-20). To increase the signal-to-noise ratio during the measurement, a lock-in amplifier (Stanford Research Systems – SR844) is implemented with input reference from the femtosecond laser. A voltage source (Agilent Technologies – E8257D) is used to apply external electric field to the device.

First, we check our device's $\chi^{(2)}$ performance without any bias voltage. Figure 4b shows the SHG emission spectrum under a 920 nm laser pulse with normal incidence. Solid red diamonds are experimental results, which are fitted by a gaussian-shaped function (blue line). Inset of Figure 4b shows the power relation between measured second-harmonic counts and input power of the laser. The fitting curve is exponential to the power of 2.0, which helps us confirm that the signal we collect is indeed all from second-order nonlinear process. Figure 4c shows measured wavelength-dependent SHG power efficiency at the incident peak intensity of 10 GW cm^{-2}, where solid red diamonds are experimental results with error-bar and blue line is a fitting curve. Since the absorption peak of plasmonic absorber is tailored to align with the $\chi^{(2)}$ peak of the cMQWs, SHG efficiency reaches its maximum at 920 nm.

Next, we demonstrate $\chi^{(2)}$ tunability at 920 nm by measuring voltage-dependent SHG intensity at 460 nm. Since SHG is a solely second-order nonlinear process, SHG intensity can be interpreted as $\chi^{(2)}$ strength. In Figure 4d, as bias voltage increases, $\chi^{(2)}$ decreases due to ISBTs misalignment caused by external electric field. When bias voltage reaches 6 V, which corresponds to an electric field magnitude of 3 MV cm^{-1} across our device, $\chi^{(2)}$ strength drops to 0.37 of its original value. This results in a modulation depth of 63% and an average tunability of 10.5% per volt. Experimental result (solid red diamonds) agrees well with theoretical prediction (blue line). Furthermore, we utilize $\chi^{(2)}$ adaptability to demonstrate electro-optic modulation of SHG signal. Figure 4e shows continuous tuning of $\chi^{(2)}$, which is observed as switching SHG signal "HIGH" and "LOW" over a long period of time. When the applied voltage is absent, intrinsically perfectly aligned double resonant transition of ISBTs inside cMQWs provides maximum $\chi^{(2)}$, and SHG signal is turned "HIGH". With the presence of applied voltage, external electric field offsets the ISBTs double resonance alignment and reduces $\chi^{(2)}$, which results in low SHG signal or switching to the "LOW" state. Note that here we use an AC voltage source, where the peak-to-peak voltage of 6 V is equivalent to the DC root-mean-square voltage of 2.12 V. More details of experimental settings are described in

ADVANCED OPTICAL MATERIALS
www.advopticalmat.de

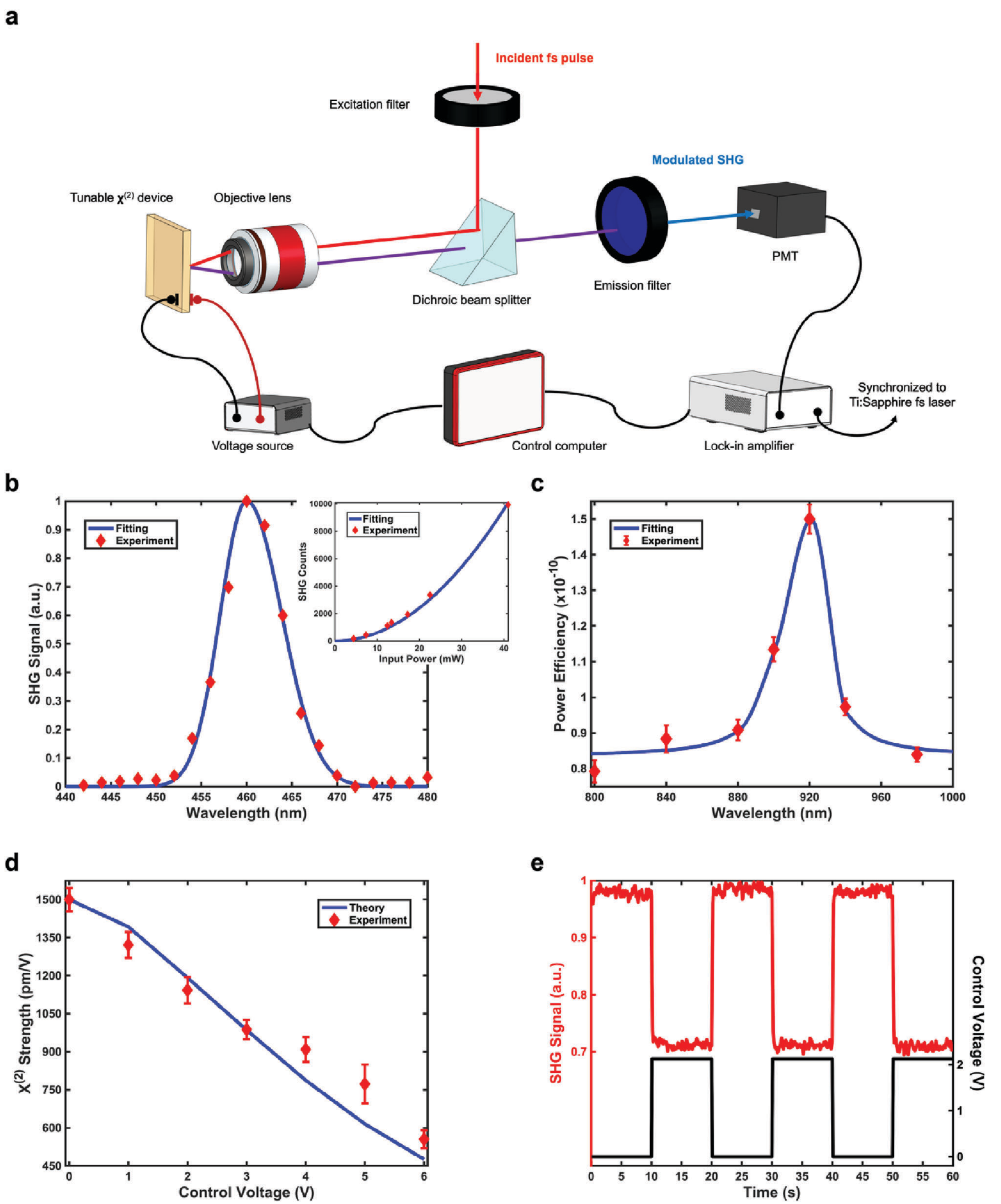

Figure 4. Optical measurement setup and result for the tunable $\chi^{(2)}$ device. a) Optical setup for the tunable $\chi^{(2)}$ measurement. b) SHG emission spectrum under a 920 nm laser pulse. Inset: power relation between measured SHG counts and input power of the laser. The fitting curve is exponential to the power of 2.0. c) Wavelength-dependent SHG power efficiency under incident pulse intensity of 10 GW cm^{-2}. d) Tunability of $\chi^{(2)}$ with respect to externally applied control voltage. Average tunability is 10.5% per volt. e) Electro-optic modulation of SHG signal based on adaptability of $\chi^{(2)}$ with modulating bias voltage. Measured SHG intensity (red line) is at HIGH state when external bias voltage (black line) is off, while SHG intensity is switched to LOW state when bias voltage is turned on. Stability proven across a time period of 60 s.

the supplementary section. Under 2.12 V, measured "LOW" state can reach down to 0.7, with normalization to "HIGH" state. In other words, we have achieved a 30% modulation depth of nonlinear SHG signal with high stability. Data are collected across a time period of 60 s to prove stability. In terms of modulation speed, since the response time of ISBTs is in few-femtosecond level, which is orders of magnitude faster than the RC time constants of electro-optic devices up to date, the switching speed of our device is essentially limited by the RC time constant of the biasing circuit. Our discoveries offer a competitive candidate for compact high-speed optical modulators in the future.

3. Conclusion

In summary, we have successfully demonstrated a quantum-engineered optical device with electrically tunable nonlinearity working at NIR wavelength. Ultrahigh $\chi^{(2)}$ of 1500 pm V^{-1} at 920 nm can be tuned with a modulation depth of 63% and an average tunability of 10.5% per volt. Electro-optic modulation of nonlinear SHG signal at 460 nm is shown with 30% modulation depth under 2.12 V biasing with high stability. Our material system can be further integrated to build a more advanced nonlinear optical device. For example, since the intrinsic giant nonlinearity originates from ISBTs, which has response speed in hundreds of terahertz level, this quantum-well-based material system is obviously one of the best candidates for a high-speed modulator. Another example is a compact optical device with programmable nonlinearity. We can achieve spatial control of optical nonlinearity, such that the nonlinear response of an incoming light field can be controlled and modulated pixel-by-pixel at individual nanogrid level. Our research paves the way for developing modern ultrafast and ultra-compact photonic system equipped with actively controllable nonlinearity.

Supporting Information

Supporting Information is available from the Wiley Online Library or from the author.

Acknowledgements

The authors acknowledge partial financial support from the National Science Foundation (NSF-ECCS-1907423).

Conflict of Interest

The authors declare no conflict of interest.

Author Contributions

C.-F.C. and H.Q. contributed equally to this work. Z.L. conceived the idea. C.-F.C. and H.Q. performed the theoretical calculation. C.-F.C. simulated and fabricated the device. C.-F.C. and H.Q. conducted the optical measurement and analyzed the experimental data. C.-F.C. prepared the manuscript. All authors revised the manuscript. Z.L. supervised the research.

Data Availability Statement

The data that support the findings of this study are available from the corresponding author upon reasonable request.

Keywords

metallic quantum wells, optical nonlinearity, tunable optical nonlinearity, tunable second-harmonic generation

Received: September 6, 2023
Revised: November 17, 2023
Published online:

[1] R. W. Boyd, *Nonlinear Optics*, 3rd Ed. Academic Press, **2008**.
[2] M. M. Fejer, S. J. B. Yoo, R. L. Byer, A. Harwit, J. S. Harrisjr, *Phys. Rev. Lett.* **1989**, *62*, 1041.
[3] R. Atanasov, F. Bassani, V. M. Agranovich, *Phys. Rev. B* **1994**, *50*, 7809.
[4] E. Rosencher, A. Fiore, B. Vinter, V. Berger, P.h. Bois, J. Nagle, *Science* **1996**, *271*, 168.
[5] C. Sirtori, F. Capasso, D. L. Sivco, A. L. Hutchinson, A. Y. Cho, *Appl. Phys. Lett.* **1992**, *60*, 151.
[6] F. Capasso, C. Sirtori, A. Y. Cho, *IEEE J. Quantum Electron.* **1994**, *30*, 1313.
[7] J. Lee, M. Tymchenko, C. Argyropoulos, P.-Y. Chen, F. Lu, F. Demmerle, G. Boehm, M.-C. Amann, A. Alù, M. A. Belkin, *Nature* **2014**, *511*, 65.
[8] J. Lee, N. Nookala, J. S. Gomez-Diaz, M. Tymchenko, F. Demmerle, G. Boehm, M.-C. Amann, A. Alù, M. A. Belkin, *Adv. Opt. Mater.* **2016**, *4*, 664.
[9] N. Nookala, J. Lee, M. Tymchenko, J. Sebastian Gomez-Diaz, F. Demmerle, G. Boehm, K. Lai, G. Shvets, M.-C. Amann, A. Alu, M. Belkin, *Optica* **2016**, *3*, 283.
[10] N. Nookala, J. Xu, O. Wolf, S. March, R. Sarma, S. Bank, J. Klem, I. Brener, M. Belkin, *Appl. Phys. B: Lasers Opt.* **2018**, *124*, 7.
[11] Y. Liu, J. Lee, S. March, N. Nookala, D. Palaferri, J. F. Klem, S. R. Bank, I. Brener, M. A. Belkin, *Adv. Opt. Mater.* **2018**, *6*, 6.
[12] J. Yu, S. Park, I. Hwang, D. Kim, F. Demmerle, G. Boehm, M.-C. Amann, M. A. Belkin, J. Lee, *Nat. Photon.* **2022**, *16*, 72.
[13] R. Yu, J. D. Cox, F. J. G. De Abajo, *Phys. Rev. Lett.* **2016**, *117*, 123904.
[14] E. Brown, T. Mckee, E. Ditomaso, A. Pluen, B. Seed, Y. Boucher, R. K. Jain, *Nat. Med.* **2003**, *9*, 796.
[15] P. J. Campagnola, L. M. Loew, *Nat. Biotechnol.* **2003**, *21*, 1356.
[16] J. Butet, K. Thyagarajan, O. J. F. Martin, *Nano Lett.* **2013**, *13*, 1787.
[17] X. Yin, Z. Ye, D. A. Chenet, Y. Ye, K. O'brien, J. C. Hone, X. Zhang, *Science* **2014**, *344*, 488.
[18] S. Shen, L. Meng, Y. Zhang, J. Han, Z. Ma, S. Hu, Y. He, J. Li, B. Ren, T.-M. Shih, Z. Wang, Z. Yang, Z. Tian, *Nano Lett.* **2015**, *15*, 6716.
[19] R. S. Jacobsen, K. N. Andersen, P. I. Borel, J. Fage-Pedersen, L. H. Frandsen, O. Hansen, M. Kristensen, A. V. Lavrinenko, G. Moulin, H. Ou, C. Peucheret, B. Zsigri, A. Bjarklev, *Nature* **2006**, *441*, 199.
[20] B. Chmielak, M. Waldow, C. Matheisen, C. Ripperda, J. Bolten, T. Wahlbrink, M. Nagel, F. Merget, H. Kurz, *Opt. Express* **2011**, *19*, 17212.
[21] L.i Chen, Q. Xu, M. G. Wood, R. M. Reano, *Optica* **2014**, *1*, 112.
[22] J. Chiles, S. Fathpour, *Optica* **2014**, *1*, 350.
[23] C. Wang, M. Zhang, X.i Chen, M. Bertrand, A. Shams-Ansari, S. Chandrasekhar, P. Winzer, M. Loncar, *Nature* **2018**, *562*, 101.
[24] H. Qian, S. Li, C.-F. Chen, S.-W. Hsu, S. E. Bopp, Q. Ma, A. R. Tao, Z. Liu, *Light: Sci. Appl.* **2019**, *8*, 13.
[25] H. Qian, S. Li, Y. Li, C.-F. Chen, W. Chen, S. E. Bopp, Y.-U. Lee, W. Xiong, Z. Liu, *Sci. Adv.* **2020**, *6*, 3456.

[26] W. Cai, A. P. Vasudev, M. L. Brongersma, *Science* **2011**, *333*, 1720.
[27] L. Kang, Y. Cui, S. Lan, S. P. Rodrigues, M. L. Brongersma, W. Cai, *Nat. Commun.* **2014**, *5*, 4680.
[28] H.-H. Lin, F. Vallini, M.-H. Yang, R. Sharma, M. W. Puckett, S. Montoya, C. D. Wurm, E. E. Fullerton, Y. Fainman, *Sci. Rep.* **2017**, *7*, 9983.
[29] W. Ding, L. Zhou, S. Y. Chou, *Nano Lett.* **2014**, *14*, 2822.
[30] M.-L. Ren, J. S. Berger, W. Liu, G. Liu, R. Agarwal, *Nat. Commun.* **2018**, *9*, 186.
[31] K. L. Seyler, J. R. Schaibley, P. Gong, P. Rivera, A. M. Jones, S. Wu, J. Yan, D. G. Mandrus, W. Yao, X. Xu, *Nat. Nanotechnol.* **2015**, *10*, 407.
[32] H. Yu, D. Talukdar, W. Xu, J. B. Khurgin, Q. Xiong, *Nano Lett.* **2015**, *15*, 5653.
[33] J. Klein, J. Wierzbowski, A. Steinhoff, M. Florian, M. Rösner, F. Heimbach, K. Müller, F. Jahnke, T. O. Wehling, J. J. Finley, M. Kaniber, *Nano Lett.* **2017**, *17*, 392.
[34] X. Wen, W. Xu, W. Zhao, J. B. Khurgin, Q. Xiong, *Nano Lett.* **2018**, *18*, 1686.
[35] H. Qian, Y. Xiao, Z. Liu, *Nat. Commun.* **2016**, *7*, 13153.